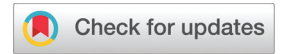
Nanoscale



PAPER



Cite this: Nanoscale, 2021, 13, 17547

Bending and precipitate formation mechanisms in epitaxial Ge-core/GeSn-shell nanowires†

Andrew C. Meng, ¹ Yanming Wang, ¹ b,c Michael R. Braun, ^a J. Zach Lentz, ^a Siying Peng, ^a Huikai Cheng, ^d Ann F. Marshall, ^e Wei Cai^f and Paul C. McIntyre*

Core-shell Ge/GeSn nanowires provide a route to dislocation-free single crystal germanium-tin alloys with desirable light emission properties because the Ge core acts as an elastically compliant substrate during misfitting GeSn shell growth. However, the uniformity of tin incorporation during reduced pressure chemical vapor deposition may be limited by the kinetics of mass transfer to the shell during GeSn growth. The balance between Sn precursor flux and available surfaces for GeSn nucleation and growth determines whether defects are formed and their type. On the one hand, when the Sn precursor delivery is insufficient, local variations in Sn arrival rate at the nanowire surfaces during GeSn growth produce asymmetries in shell growth that induce wire bending. This inhomogeneous elastic dilatation due to the varying composition occurs via deposition of Sn-poor regions on some of the {112} sidewall facets of the nanowires. On the other hand, when the available nanowire surface area is insufficient to accommodate the arriving Sn precursor flux, Sn-rich precipitate formation results. Between these two extremes, there exists a regime of growth conditions and nanowire densities that permits defect-free GeSn shell growth.

Received 30th June 2021, Accepted 3rd October 2021 DOI: 10.1039/d1nr04220c

rsc.li/nanoscale

Introduction

Recent demonstration of germanium-tin lasers^{1–5} and photodetectors^{6,7} have shown the promise of the material for silicon compatible photonics. Unlike the III–V materials that have traditionally been used for semiconductor light emitters, the components of which tend to either dope or react with silicon at typical processing temperatures, germanium-tin can be grown epitaxially on Si nanostructures in a manner similar to shell growth on Ge nanowires. However, the high Sn composition required to achieve a direct band gap in GeSn can complicate the growth process due to the limited equilibrium Sn solubility in Ge and the large lattice mismatch of Sn and Ge. A core–shell Ge/GeSn structure has a number of advantages as a model system for epitaxial GeSn on an elastically compliant single crystal substrate due to ease of synthesis, synergistic

Bent nanowires and nanowires with precipitates are undesirable from an applications perspective. Bending presents a number of challenges for devices because the amount and direction of bending can differ, resulting in higher sample variability due to the dependence of optoelectronic properties of GeSn on strain. In this study, we combine a systematic analysis of precursor mass transport effects on GeSn shell chemical vapor deposition with phase field simulations of the resultant inhomogeneities in growth to understand the underlying mechanisms.

In catalyzed semiconductor nanowire growth, varying the areal density of catalyst nanoparticles on the substrate surface provides one means to systematically study the effects of precursor mass transport. This approach has been used extensively in III–V nanowire growth to probe the kinetics and mechanisms of mass transport of group-III *versus* group-V gas precursors from the vapor phase to the catalyst surface. Herein, we apply this method to observe the change in bend and precipitate morphologies of core–shell Ge/GeSn nanowires under varying precursor mass transport conditions. In addition to structural characterization, optical properties of the core–shell Ge/GeSn

photonic properties, and high GeSn crystalline quality.^{8–11} Studies of GeSn shell growth have potentially wide applications in nanostructures of different geometries. Several studies suggest Sn precursor mass transport is a controlling factor for the morphology, growth mode, and Sn composition of GeSn shells grown on single crystal Ge nanowires.^{10,12,13} As a result, we focus on the influence of Sn flux on the morphology and crystalline quality of GeSn shell growth on Ge nanowires.

^aDepartment of Materials Science and Engineering, Stanford University, Stanford, CA 94305, USA. E-mail: pcm1@slac.stanford.edu

^bDepartment of Materials Science and Engineering, Massachusetts Institute of Technology, Cambridge, MA 02139, USA

^cUniversity of Michigan-Shanghai Jiao Tong University Joint Institute, Shanghai Jiao Tong University, Shanghai, China 200240

^dThermoFisher Scientific, Hillsboro, OR 97124, USA

^eStanford Nano Shared Facility, Stanford University, Stanford, CA 94305, USA

Department of Mechanical Engineering, Stanford University, Stanford, CA 94305,

 $[\]dagger\, Electronic$ supplementary information (ESI) available. See DOI: 10.1039/d1nr04220c

nanowires are characterized using photoluminescence (PL) to investigate the influence of growth-induced inhomogeneities on the wires' optoelectronic properties.

One of the main challenges to understanding bend and precipitate formation is the inability to observe structural evolution *in-situ* during chemical vapor deposition under typical reaction conditions. Therefore, phase field simulations are performed to provide insight into possible pathways for the evolution of these structures. We examine the nanowires postgrowth to characterize an observed structure, then use the phase field model to predict the degree of bending in the nanowire by linking the observed shape and composition of Sn-poor regions in the shell to the associated asymmetric elastic strain distribution. We hypothesize that bend and precipitate formation during GeSn shell growth results from locally non-uniform gas precursor mass transport, which affects the balance between the Sn precursor flux and the available surface for GeSn nucleation and growth. This hypothesis is tested by ex situ experimental observation of post-growth morphologies as a function of nanowire areal density, enabling us to better understand the shell growth mechanism.

Experimental

Germanium nanowires are grown as elastically compliant substrates for subsequent GeSn shell growth via a two-step vaporliquid-solid (VLS) process involving a nucleation step at 375 °C followed by steady-state growth at 300 °C. The reactor pressure was controlled at 30 Torr pressure throughout the growth process, with only H2 gas flowing at that pressure prior to nanowire growth. The temperature is ramped up at 5 °C s⁻¹, and GeH₄ begins flowing 6 min after the wafer surface temperature stabilizes at 375 °C. A subsequent temperature ramp down to 300 °C for steady state VLS growth of untapered Ge nanowires occurs at a rate of −1.25 °C s⁻¹. During Ge nanowire growth, the GeH₄ partial pressure is 0.47 Torr with the balance consisting of H₂. Different VLS catalyst loadings (nanoparticle areal densities) on the substrate surface are chosen to examine the effects of available Ge surface area on bend and precipitate formation during growth of the GeSn shells. To accomplish this, solutions for VLS catalyst deposition were made using 3:1 and 1:1 solutions of 40 nm citrate stabilized Au colloids (Sigma-Aldrich) in 5.9 M HF (aq) (v/v). The colloid was dropcast onto Ge (111) growth substrates (MTI, n-type, ρ =

0.005–0.01 Ω cm) following three conditions: (1) 3:1 solution, 3 × 2 min; (2) 3:1 solution, 1 × 2 min; and (3) 1:1 solution, 1 × 2 min. All GeSn shells were grown at 275 °C (ramped down from steady state Ge nanowire growth at -1.25 °C s⁻¹) with $P_{\rm SnCl_4} = 0.028$ Torr for a duration of 30 min.

Scanning electron microscope (SEM) images were obtained using an FEI Helios 600i DualBeam focused ion beam (FIB)/ SEM at an acceleration voltage of 2 kV and beam current of 43 pA. High resolution X-ray diffraction patterns were collected using a PANalytical X'Pert diffractometer with monochromated Cu $K_{\alpha 1}$ radiation \emph{via} a hybrid X-ray mirror and 2 crystal Ge (220) 2-bounce monochromator with a 3-bounce Ge (220) analyzer crystal in the diffracted beam path. Auger electron spectroscopy (AES) data was collected using a Phi 700 Scanning Auger Nanoprobe operated at 10 kV accelerating voltage and 10 nA beam current. A micro-PL setup with a 980 nm diode laser focused to an 8 µm diameter spot size with a Mitutoyo 20× M Plan NIR microscope objective (NA = 0.4) in a surface normal pump/collection geometry was used to obtain the photoluminescence (PL) data at room temperature. A Stanford Research Systems SR830 Lock-in Amplifier with a mechanical chopper at 290 Hz was used for phase sensitive detection of PL using a thermoelectric-cooled (-20 °C) extended InGaAs photodiode (EOS IGA2.2-010-TE2-H) detector with a 2.4 µm cutoff wavelength. Cross-section transmission electron microscope (TEM) samples were prepared by transferring nanowires to a Si (100) substrate and then lifting them out using the FIB/SEM. Scanning transmission electron microscope (STEM) images were collected at 300 kV accelerating voltage from a FEI Themis 60-300 kV (Hillsboro, OR) with an aberration corrector for the probe forming optics. Energy dispersive X-ray spectroscopy (EDS) was performed in STEM mode using a SuperX EDS detector.

Phase field simulations

A quasi-2D phase field model (on the nanowire cross section) coupled with linear elasticity theory was developed, adopting the formulation proposed in our previous work (more details are provided in the ESI†).^{8,12} The fundamental degrees of freedom of this model include a phase field for representing the geometry of the wire, and a displacement field for describing the elastic deformation induced by Ge/GeSn lattice mismatch. The anisotropic interfacial energies and the elastic constants measured from experiments^{16,17} were converted to the

Table 1 Parameters in the phase field model. U, ${\varepsilon_0}^2$, ${\varepsilon_1}$, ${\varepsilon_2}$ and ${\varepsilon_3}$ are the interfacial energy associated parameters for reproducing the anisotropic surface energies of Ge crystal. h is the grid size. C_{11} , C_{12} and C_{44} are the elastic constants of bulk Ge. M is the kinetic coefficient of the elasticity step. Δt and Δt_2 are the time steps for the phase field step and the elasticity step, respectively

U (eV nm ⁻³)	$\varepsilon_0^2 (\text{eV nm}^{-1})$	$arepsilon_1$	$arepsilon_2$	$arepsilon_3$	h (nm)
6.616	71.626	0.346	-3.815	-0.560	1.5
C_{11} (GPa)	C_{12} (GPa)	C ₄₄ (GPa)	$M \left(\text{nm}^4 \left(\text{eV s}^{-1} \right) \right)$	Δt (s)	Δt_2 (s)
126.0	44.0	67.7	1.0	0.072	0.0036

input model parameters (Table 1). A Sn-concentration dependent eigenstrain field was introduced, to account for the misfit strain between pure Ge and GeSn. 18 For each simulation, an initial configuration representing the core-shell nanowire cross section was created, followed by a short run to equilibrate the phase field profile across the interface. Then an eigenstrain field was assigned to describe the distribution of misfit strain, such that its pattern reasonably matched the STEM-EDS composition map of the wire cross section. Next, the displacement field is solved by iteratively minimizing the elastic energy. During the simulation, the total force and bending moment on the nanowire cross section were kept zero, which was achieved by superposing a linearly varied strain field with its magnitude auto-adjusted via a feedback loop. Finally, based on the Euler-Bernoulli beam theory, the deflection of the nanowire was calculated from the simulationpredicted out-of-plane strain distribution.

Results and discussion

Morphology

Vertical core–shell Ge/GeSn nanowire assemblies were grown on Ge (111) substrates with average nanowire areal densities of 2 μm^{-2} , 0.8 μm^{-2} , and 0.2 μm^2 (Fig. 1a–c). SEM images show that, for the sample with nanowire density of 2 μm^{-2} , a significant fraction of the nanowires exhibit pronounced bending (Fig. 1a). The bending in the nanowires, which are ~200 nm in diameter, does not change as a function of the SEM imaging conditions, indicating that it is not induced by exposure of the wires to the electron beam. The crescent shaped defect in the nanowire cross-section is often observed in the bent nanowires (Fig. 2).

This bending effect is observed to decrease as the nanowire areal density decreases and is less apparent as the average

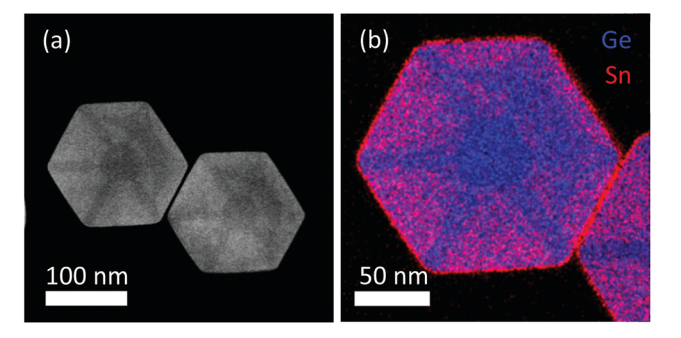


Fig. 2 Probe aberration corrected (a) HAADF-STEM image and (b) STEM-EDS map of a Sn-poor shell region in bent core—shell nanowire cross-section, and a Sn-rich sidewall surface wetting layer.

nanowire areal density on the substrate surface is reduced to 0.8 μm⁻² (Fig. 1b). Furthermore, at sufficiently low nanowire areal densities, Sn-rich precipitates are observed on both the wire and substrate surfaces after growth (Fig. 1c). The relative supply of SnCl4 precursor arriving at the surface compared to the available surface area for GeSn nucleation and growth decreases as a function of increasing nanowire density. Typical nanowires were approximately 4 µm in length, 200 nm in diameter, with core diameter of ~50 nm. For 200 nm diameter nanowires with 4 µm length, the total sample surface area per 1 μm² of substrate (projected) area increases from 1.50 μm²/ μm^2 to 3.01 $\mu m^2/\mu m^2$ to 6.02 $\mu m^2/\mu m^2$ as nanowire areal density increases from 0.2 μm^{-2} to 0.8 μm^{-2} to 2 μm^{-2} . The results suggest that local non-uniformity of the arriving Sn flux causes nanowire bending to become progressively severe under increasingly precursor mass transport limited conditions. On the other hand, Sn-rich precipitates are favored under conditions when the relative Sn precursor flux compared to the available surface for GeSn nucleation and growth is increased.

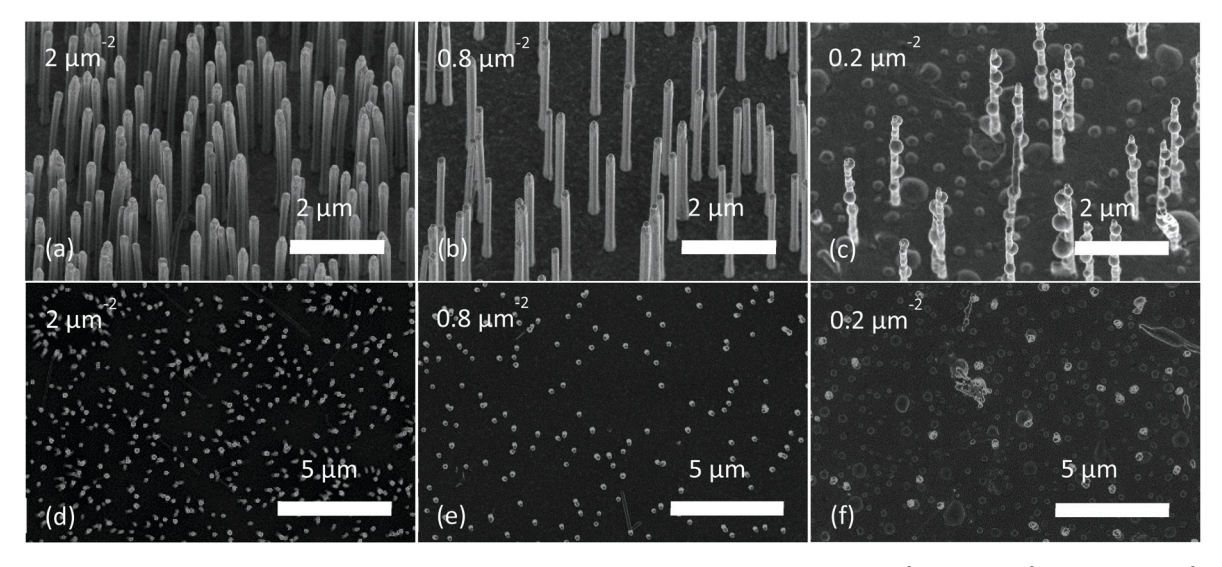


Fig. 1 Side-view SEM images of core-shell Ge/GeSn nanowires grown at nanowire densities of (a) $2 \mu m^{-2}$, (b) $0.8 \mu m^{-2}$, and (c) $0.2 \mu m^{-2}$. Top-view SEM images of core-shell Ge/GeSn nanowires grown at densities of (d) $2 \mu m^{-2}$, (e) $0.8 \mu m^{-2}$, and (f) $0.2 \mu m^{-2}$.

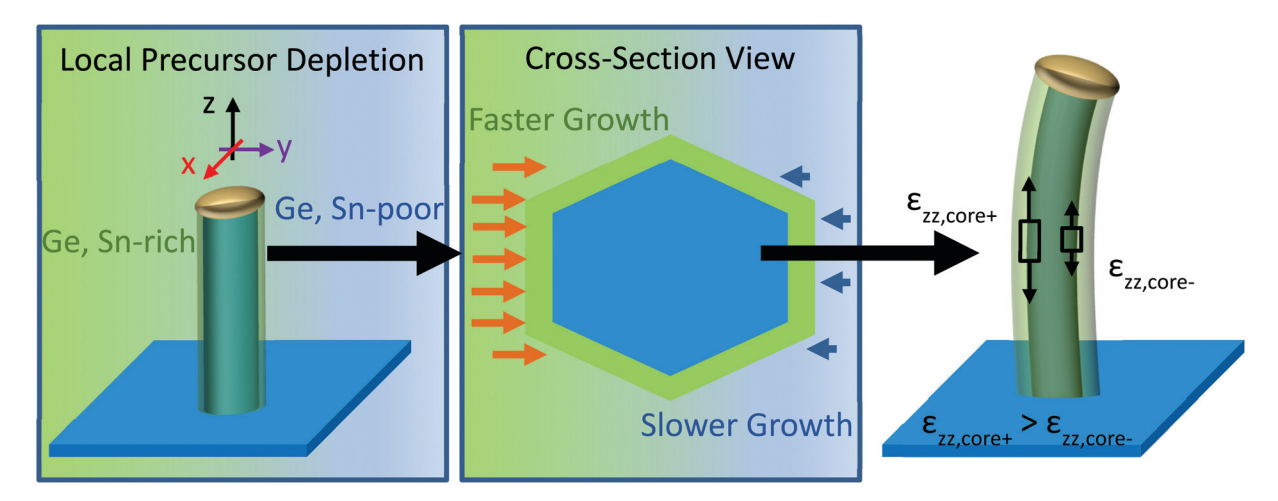
Bending mechanism

The formation of bends and precipitates can be understood as originating from a local imbalance between the gas precursor flux and the available surface sites for Ge or Sn incorporation into the growing GeSn shell. On the one hand, when local areal density of attachment sites is small (sparse nanowires), more precursor arrives at each unit area of the growth surface, resulting in a higher shell growth rate. Under high Sn flux and at the growth temperatures employed, Sn droplets presumably decorate the surface of both the shells and the field regions between the nanowires and then solidify to form the precipitates during cooling. Because GeSn alloys with Sn composition greater than ~1 at% are metastable under the growth conditions, once Sn droplets form, Sn adatoms that deposit on the substrate will preferentially incorporate in these droplets rather than in the GeSn alloy shell. In the case of low wire areal density, insufficient number of attachment sites on the GeSn alloy surface could result in a sufficiently high surface concentration of Sn to form Sn droplets (Fig. 1c). The growth of these droplets leads to a relative Sn depletion of the alloy composition compared to conditions under which Sn droplet formation is avoided.

On the other hand, bending can arise from asymmetries in growth rates on different facets of the same nanowire, an illustration of which is shown in Scheme 1. We hypothesize that under gas precursor supply limited conditions (high nanowire areal density), as opposed to adatom attachment site limited conditions, uneven precursor depletion from the gas around the shell surface leads to differences in GeSn shell growth rate on the various nanowire sidewall facets. Because CVD is not a line-of-sight process, shadowing will not occur in the same sense that it would in many physical vapor deposition processes, for example. However, the presence of nanowires and differences in local nanowire density could affect the diffusion length of the atoms on the substrate and nanowire surface due

to the nanowires acting as sinks for Ge and Sn adatoms. If the bending is random with respect to each NW's surroundings, that would suggest that stochastic localized depletion of precursor relative to the available surface site density would be responsible for initiating the bending instability, which is selfreinforcing. On the other hand, if there are locally more sites for adatom attachment competing for a given incoming flux of adatoms (Ge or Sn) than the average site density, then the precursor supply may be depleted locally and this will lead to a slower growth rate. For example, wires clustered close together would tend to bend toward one-another in that circumstance. The data are consistent with the latter situation, as wires clustered close together tend to bend toward one another (Fig. 1d). Uneven growth rates on diametrically opposing facets will lead to a bending moment that results in tensile and compressive strains on the outside and inside of the bend, thus favoring growth of Sn-rich and Sn-poor regions, respectively. This is consistent with the observed concentration profiles in a bent nanowire cross-section (Fig. 2). The Sn to Ge ratio should not vary significantly at the onset of growth if well-mixed gas precursors are assumed; therefore, growth rate asymmetry induced bending provides a consistent explanation of the observed bending. Another factor is the difference in the molar masses of GeH₄ (76.6 g mol⁻¹) and SnCl₄ (260.5 g mol⁻¹). According to kinetic molecular theory, gas diffusion coefficients scale with the inverse square root of the molar mass. Therefore, the local supply of Sn to the growing shell surface may be more likely to suffer from a diffusion limitation than is Ge. Wire bending due to local gas-phase precursor depletion is consistent with prior observations suggesting that VLS growth of Ge nanowires and growth of GeSn shells in this CVD reactor can be precursor mass transport limited. 19,20

To understand the structural and composition changes within the nanowire associated with shell growth that produces bent core-shell Ge/GeSn nanowires, cross-section high-



Scheme 1 Formation of bend in core-shell Ge/GeSn nanowire. Local SnCl₄ concentration gradients arising from poor mass transport lead to asymmetric growth and inhomogeneous axial core-shell strain, $\varepsilon_{zz,core}$. The side of the nanowire with higher GeSn growth rate will experience a higher core-shell strain, $\varepsilon_{zz,core+}$ than the side with lower GeSn growth rate ($\varepsilon_{zz,core-}$).

angle annular dark field (HAADF) STEM imaging and EDS mapping were performed. HAADF-STEM images highlight the contrast between high and low atomic number (Z) elements. While a non-bent core-shell nanowire with six facets and spokes exhibits approximately three-fold symmetry, 8,21 bending breaks this symmetry. The nanowire cross section structure used as the input for phase field simulations (vide infra) is adapted from the experimental results as observed in the HAADF-STEM image and through STEM-EDS composition mapping (Fig. 2). The image in Fig. 2a shows that bent nanowires exhibit a crescent-shaped low Z region parallel to a {112} facet, corresponding to a Sn-poor region emanating from one {112} sidewall facet of the nanowire as observed in the STEM-EDS map. A possible mechanism for Sn depletion induced bending is that a Sn-poor region will have a higher lattice mismatch with higher Sn composition GeSn and vice versa. Once a Sn-poor region forms, the gradient of Sn composition across the shell surface will produce a locally varying energy barrier to Sn incorporation that results in asymmetric growth and bending.

To test whether an asymmetric shell growth rate could cause bending of the nanowire independent of Sn-poor regions, we use the phase field model to simulate shell growth on a nanowire with an asymmetric cross-section and off-center core similar to those observed in Fig. 2, but without a crescent shaped Sn deficient region. This is done to assess the effect of asymmetric GeSn shell growth rates. The nanowire deflection, axial strain distribution, and strain energy density distribution are shown in Fig. 3a-c. We also verified that no bending occurs in a symmetric core-shell nanowire in which the growth rates are the same on each facet (ESI Fig. S1†). Even with no Sn-poor region in the shell, a bending moment resulting from the assumed asymmetric GeSn shell growth results. The bending moment produces asymmetric elastic strain of the surface facet planes on either side of the nanowire, and this may serve to initiate the growth of a Sn-poor shell region on the side that exhibits greater compressive strain.

Taking the bent nanowire configuration as the initial condition, we perform a series of simulations (shown in Fig. 4a-i)

in which the elastic energy is evaluated when the Sn composition is varied in a crescent-shaped Sn-poor region of the shell similar to what is observed in our experiment (the rest of the GeSn shell is simulated as having a uniform 9 at% Sn). As a function of increasing Sn composition in the crescentshaped Sn-poor region, the elastic energy of the nanowire first decreases, then increases again, with the energy minimum occurring near 6 at% Sn (Fig. 4j). This shows that the experimentally observed crescent shaped Sn-poor regions having intermediate Sn composition greater than that of the Ge core, but less than that of the non-depleted regions of the GeSn shell, are favored from an elastic energy standpoint. The compressive strain that arises on the inside of the nanowire bend, where these regions form, would tend to favor lower Sn concentrations, consistent with results of both experiment and simulation.

In summary, the mechanism for bending can be understood as a shell growth instability similar to nanowire kinking, except that the process is caused by an asymmetric radial shell growth, likely resulting from local precursor depletion in the gas phase around the nanowires, that promotes formation of Sn-poor regions in the shell.

Sn-Rich precipitates

To understand the properties of Sn-rich precipitates and factors that influence their formation, additional structural and optical property characterization was performed. High-resolution X-ray diffraction symmetric scans show that the Sn composition of the shell decreases as the nanowire areal density on the substrate surface increases from $0.8 \ \mu m^{-2}$ to $2 \ \mu m^{-2}$, but it increases as the areal density increases from $0.2 \ \mu m^{-2}$ to $0.8 \ \mu m^{-2}$ (Fig. 5a and Table 2). This reflects a change from Sn precursor supply limited growth, in which wire bending occurs *in extremis*, to adatom attachment site limited growth, in which precipitate defects may be observed. The GeSn (333) peaks in Fig. 5a are very broad for high wire areal densities because many of the nanowires are bent: if we consider a 200 nm diameter nanowire with a bending radius of $10 \ \mu m$, the axial lattice parameter variation is approximately

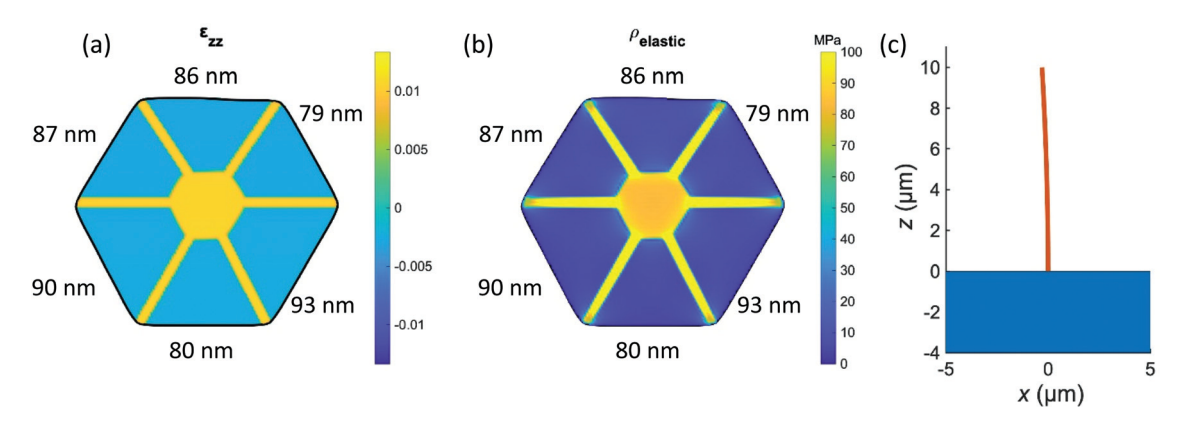


Fig. 3 Simulation of bending in an asymmetric core-shell Ge/GeSn nanowire with a nominal 9 at% Sn composition in the GeSn shell and no crescent shaped (Fig. 2) Sn-poor region: (a) axial strain, (b) elastic energy density, and (c) nanowire deflection. In (a) and (b), facet lengths in nm are indicated.

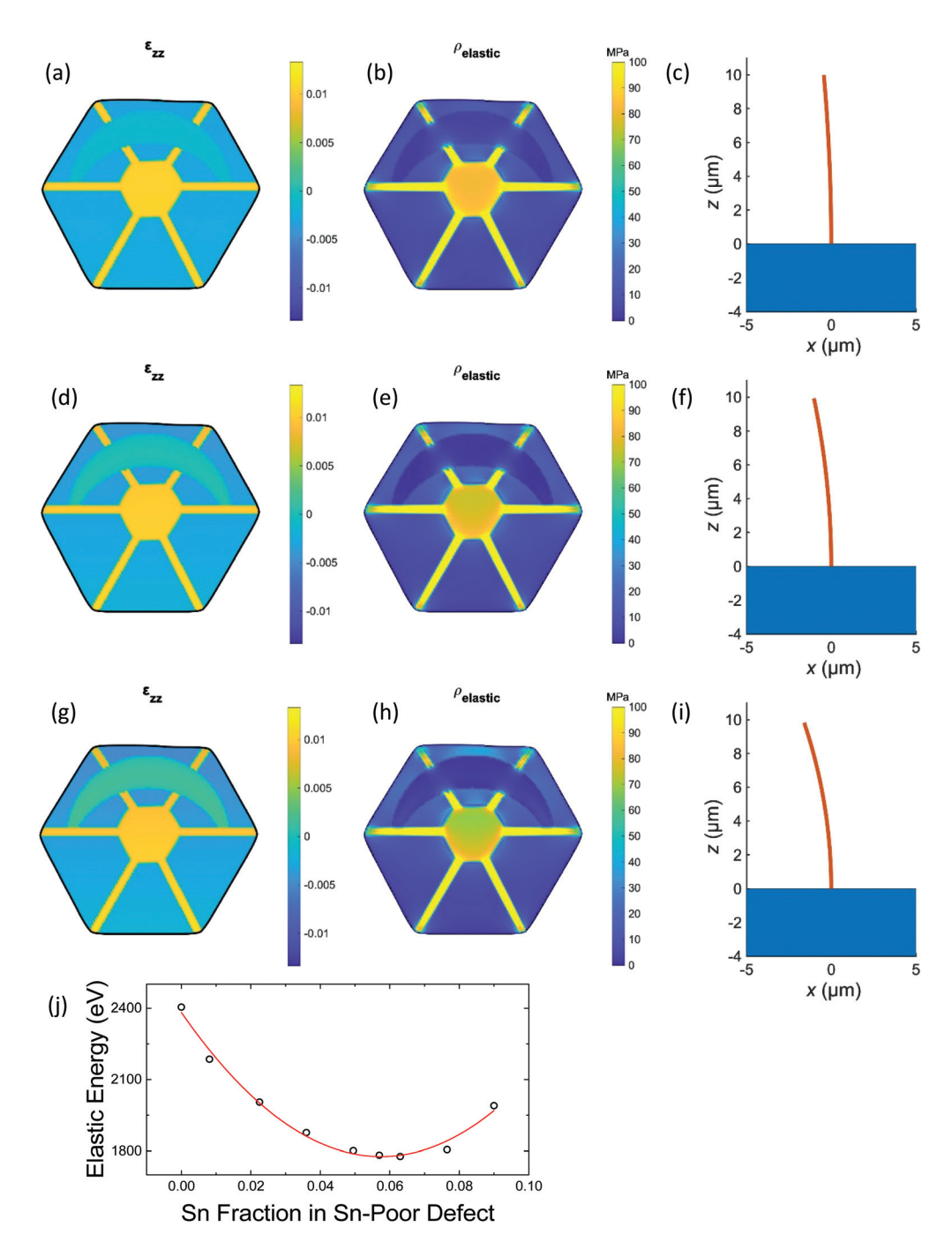
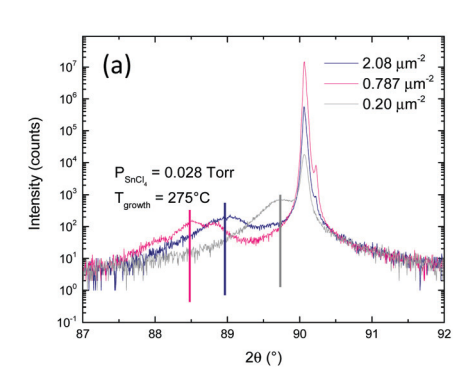


Fig. 4 Simulation of bending in asymmetric core—shell Ge/GeSn with a nominal 9 at% Sn composition in the GeSn shell and crescent shaped Sn-poor region with 7.7 at% Sn in Sn-poor region: (a) axial strain, (b) elastic energy density, and (c) nanowire deflection; with 6.3 at% Sn in Sn-poor region (d) axial strain, (e) elastic energy density, and (f) nanowire deflection, and with 5.0 at% Sn in Sn-poor region (g) axial strain, (h) elastic energy density, and (i) nanowire deflection; (j) elastic energy as a function of the Sn composition of a crescent shaped Sn-poor region.

linearly distributed from -1% to 1%, corresponding to a full width half maximum of roughly 1° (Fig. S2†). Three overlapping GeSn (333) peaks evident at intermediate wire areal densities (Fig. 5a, pink trace) have been described previously and attributed to variations in shell composition along the wire axis.²⁰ For the purpose of calculating the Sn composition of the nanowire, the highest intensity peak corresponding to the

majority volume fraction of the nanowire is used. Detailed fitting of the 2θ angles for the GeSn shell (333) peaks and calculation of the Sn composition is shown in the ESI (Fig. S3†). Because a majority of the coherent core–shell strain is stored in the core, which experiences significant axial tension, the out-of-plane lattice spacing in the GeSn shell is very close to its equilibrium value: as a result, the compositions can be esti-



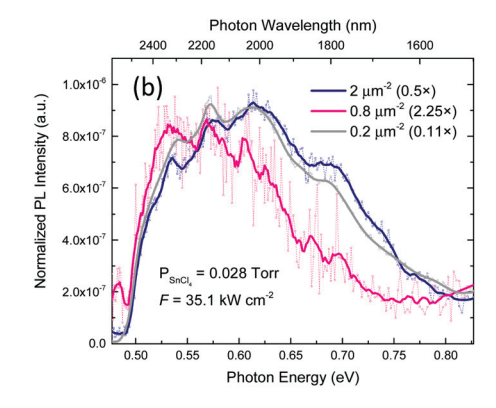


Fig. 5 (a) High resolution X-ray diffraction symmetric scan of (333) substrate and nanowire peaks, (b) photoluminescence from core—shell Ge/GeSn nanowires transferred onto Si/native oxide substrates.

Table 2 Summary of structural and morphological changes due to VLS catalyst loading

Nanowire areal density	2θ, GeSn (333) ^a	XRD-derived Sn composition ^a	Bending	Precipitates
0.2 μm ⁻²	88.957°	1.9 at%	None	Yes
0.8 μm ⁻²	88.485°	10 at%	Slight	No
2 μm ⁻²	89.752°	6.9 at%	Significant	No

 $[^]a$ 2θ and composition values from Fig. 5a corresponding to the marked peaks.

mated assuming an approximately relaxed GeSn shell and applying Vegard's Law. 8,13 Photoluminescence spectra detected from core–shell Ge/Ge $_{1-x}\mathrm{Sn}_x$ nanowires transferred onto non-photoactive Si/native oxide substrates show that light emission from the $0.8~\mu\mathrm{m}^{-2}$ sample exhibits the lowest photon

energy, reflecting its higher Sn composition, while the $2~\mu m^{-2}$ and $0.2~\mu m^{-2}$ samples exhibit similar photoluminescence despite very different Sn compositions incorporated in the GeSn shells (6.9 at% and 1.9 at%, respectively), as inferred from the XRD data (Fig. 5a). Auger electron spectroscopy maps (Fig. 6a) and cross-section STEM EDS (Fig. 6b and c) confirm that the precipitates are Sn rich. In addition, the Sn content in the nanowires with precipitates is significantly non-uniform as shown in Fig. 6c.

The increase in the Sn composition of the GeSn shell as the nanowire density decreases from 2 μm^{-2} to 0.8 μm^{-2} is consistent with expectations that local Sn precursor depletion (due to higher nanowire areal density) lowers the average Sn composition of the nanowire assembly. These results are summarized in Table 2. However, the observed decrease in Sn composition of the shell as nanowire areal density further decreases from 0.8 μm^{-2} to 0.2 μm^{-2} (which increases Sn precursor flux per

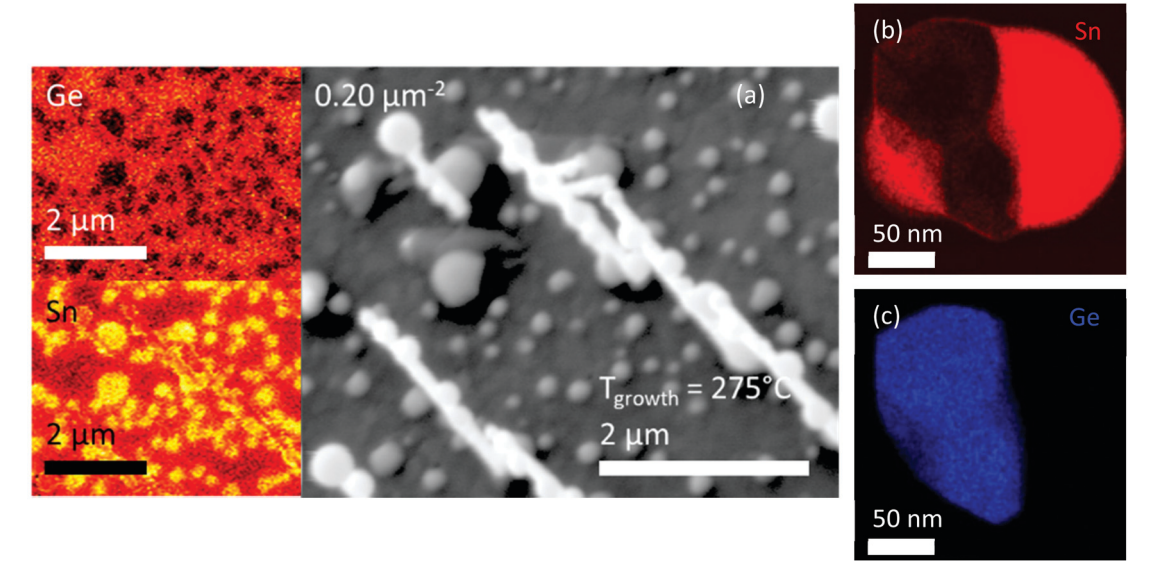


Fig. 6 (a) Auger electron spectroscopy map of Sn precipitates, (b and c) cross-section STEM-EDS of two nanowires that have grown together with precipitates.

unit sample surface area) can be ascribed to more Sn in randomly crystallographically oriented precipitates and less in the nanowire. The reduced Sn incorporation in the shell in the $0.2~\mu m^{-2}$ nanowire areal density sample is consistent with the large mass of Sn stored in precipitates that decorate the sample surface. We hypothesize that under adatom attachment site limited conditions, when the nanowire areal density on the substrate surface is low, the GeSn shell growth rate is insufficient to permit Sn solute trapping in the diamond cubic phase at the shell growth front, thus producing Sn-rich precipitates on the surface.

One important note for the PL data is that the detector used has a 2.4 µm wavelength cutoff. As the spectra of each of the samples shows significant intensity up to the detector cutoff, it is likely that all of these samples exhibit emission at wavelengths longer than 2.4 µm that is not detected. For nanowires transferred from the highest wire areal density sample (2 μm^{-2}), the PL has higher energy photon emission due to the Sn poor regions in the bent nanowire cross-sections. The spectrum is complicated due to variation of compositions and strain states, as evidenced by the STEM-EDS characterization in Fig. 2b and phase field modeling in Fig. 3 and 4. Nanowires transferred from the intermediate density sample (0.8 μ m⁻²) exhibit features at lower photon energies ranging from 0.53 eV and 0.61 eV, respectively (Fig. 5b). Wires with the lowest areal densities on the growth substrate (0.2 μ m⁻²) and decorated by Sn-rich precipitates, exhibit anomalous PL inconsistent with the measured Sn composition. We attribute emission below ~0.57-0.58 eV to Γ-valley recombination and emission at higher photon energies to L-valley recombination.8,22,23 It is possible that the PL emission from these nanowires is affected by local variation of Sn composition of the GeSn shells arising from the presence of Sn precipitates—radiative recombination would occur preferentially in regions of smaller band gap (higher Sn composition) compared to the average value. Furthermore, the shell thickness in the presence of Sn precipitates may be thinner than for the other conditions, resulting in compressive strain that would cause an underestimation of Sn composition from XRD. For bent nanowires, the extremely broad emission features can be explained by the linear axial strain distribution from approximately -1% to 1% across the wire radius (Fig. S2†). For nanowires decorated by precipitates, these broad emission features may result from the highly varying Sn composition across the GeSn shell in the presence of the precipitates (Fig. 6c).9

Conclusion

These experiments in $Ge\text{-}core/Ge_{1-x}Sn_x\text{-}shell$ nanowire synthesis demonstrate that the surface area available for atom attachment, which depends strongly on the wire areal density on the growth substrate, is an important factor in high quality $Ge_{1-x}Sn_x$ shell growth under precursor mass transport-limited conditions. When the Sn gas precursor supply is too low compared to the available surface area for adatom attachment, the

core/shell nanowires bend and exhibit Sn-poor shell compositions on the concave regions of the bend. This is consistent with SnCl₄ depletion due to limited mass transport to the nanowire surface leading to growth of Sn-poor regions of the shell. The bending instability is self-reinforcing, as Sn-poor regions exhibit a significant elastic energy barrier for Sn atom incorporation once they form. Sn phase separation at very low nanowire densities arises due to high Sn precursor flux compared to the available surface for GeSn nucleation and growth. These results show that growth of GeSn shells on Ge nanowires requires a balance between the Sn precursor flux and the available area for GeSn nucleation and growth.

Conflicts of interest

There are no conflicts to declare.

Acknowledgements

ACM would like to acknowledge funding from NSF GRFP award DGE-114747 and an ARCS Foundation Fellowship. YW would like to acknowledge funding from the National Natural Science Foundation of China (Grant No. 5210020146). This work was supported by the National Science Foundation Division of Materials Research program DMR-1608927 and DMR-2003266. Part of this work was performed at the Stanford Nano Shared Facilities supported by the National Science Foundation under award ECCS-1542152. MRB would like to acknowledge financial support from NSF GRFP award DGE-1656518.

References

- V. Reboud, A. Gassenq, N. Pauc, J. Aubin, L. Milord,
 Q. M. Thai, M. Bertrand, K. Guilloy, D. Rouchon,
 J. Rothman, T. Zabel, F. Armand Pilon, H. Sigg,
 A. Chelnokov, J. M. Hartmann and V. Calvo, Appl. Phys. Lett., 2017, 111, 092101.
- W. Dou, Y. Zhou, J. Margetis, S. A. Ghetmiri, S. Al-Kabi,
 W. Du, J. Liu, G. Sun, R. A. Soref, J. Tolle, B. Li,
 M. Mortazavi and S.-Q. Yu, Opt. Lett., 2018, 43, 4558-4561.
- 3 D. Stange, S. Wirths, R. Geiger, C. Schulte-Braucks, B. Marzban, N. von den Driesch, G. Mussler, T. Zabel, T. Stoica, J.-M. Hartmann, S. Mantl, Z. Ikonic, D. Grützmacher, H. Sigg, J. Witzens and D. Buca, ACS Photonics, 2016, 3, 1279–1285.
- 4 A. Elbaz, D. Buca, N. von den Driesch, K. Pantzas, G. Patriarche, N. Zerounian, E. Herth, X. Checoury, S. Sauvage, I. Sagnes, A. Foti, R. Ossikovski, J.-M. Hartmann, F. Boeuf, Z. Ikonic, P. Boucaud, D. Grützmacher and M. El Kurdi, *Nat. Photonics*, 2020, 14, 375–382.
- 5 J. Chrétien, N. Pauc, F. Armand Pilon, M. Bertrand, Q.-M. Thai, L. Casiez, N. Bernier, H. Dansas, P. Gergaud,

E. Delamadeleine, R. Khazaka, H. Sigg, J. Faist, A. Chelnokov, V. Reboud, J.-M. Hartmann and V. Calvo, *ACS Photonics*, 2019, **6**, 2462–2469.

- 6 J. Werner, M. Oehme, M. Schmid, M. Kaschel, A. Schirmer, E. Kasper and J. Schulze, *Appl. Phys. Lett.*, 2011, 98, 061108.
- 7 Y. Dong, W. Wang, D. Lei, X. Gong, Q. Zhou, S. Y. Lee, W. K. Loke, S.-F. Yoon, E. S. Tok, G. Liang and Y.-C. Yeo, Opt. Express, 2015, 23, 18611–18619.
- 8 A. C. Meng, M. R. Braun, Y. Wang, C. S. Fenrich, M. Xue, D. R. Diercks, B. P. Gorman, M. I. Richard, A. F. Marshall, W. Cai, J. S. Harris and P. C. McIntyre, *Mater. Today Nano*, 2019, 5, 100026.
- 9 A. C. Meng, C. S. Fenrich, M. R. Braun, J. P. McVittie, A. F. Marshall, J. S. Harris and P. C. McIntyre, *Nano Lett.*, 2016, 16, 7521–7529.
- 10 S. Assali, R. Bergamaschini, E. Scalise, M. A. Verheijen, M. Albani, A. Dijkstra, A. Li, S. Koelling, E. P. A. M. Bakkers, F. Montalenti and L. Miglio, ACS Nano, 2020, 14, 2445–2455.
- 11 M. Albani, S. Assali, M. A. Verheijen, S. Koelling, R. Bergamaschini, F. Pezzoli, E. P. A. M. Bakkers and L. Miglio, *Nanoscale*, 2018, **10**, 7250–7256.
- 12 Y. Wang, A. C. Meng, P. C. McIntyre and W. Cai, *Nanoscale*, 2019, 11, 21974–21980.
- 13 A. C. Meng, Ph.D., Stanford University, 2019.

- 14 Y. Kim, H. J. Joyce, Q. Gao, H. H. Tan, C. Jagadish, M. Paladugu, J. Zou and A. A. Suvorova, *Nano Lett.*, 2006, 6, 599–604.
- 15 I. Miccoli, P. Prete and N. Lovergine, *CrystEngComm*, 2015, 17, 5998–6005.
- 16 R. J. Jaccodine, J. Electrochem. Soc., 1963, 110, 524.
- 17 S. Nikanorov and B. K. Kardashev, *Moscow Izdatel Nauka*, 1985, https://scholar.google.com/scholar?hl=en&as_sdt=0%2C39&q= SP+Nikanorov%2C+BK+Kardashev+-+Moscow+Izdatel+Nauka% 2C+1985&btnG=.
- 18 N. Bhargava, M. Coppinger, J. P. Gupta, L. Wielunski and J. Kolodzey, *Appl. Phys. Lett.*, 2013, **103**, 041908.
- 19 S. V. Thombare, A. F. Marshall and P. C. McIntyre, APL Mater., 2013, 1, 061101.
- 20 A. C. Meng, M. R. Braun, Y. Wang, S. Peng, W. Tan, J. Z. Lentz, M. Xue, A. Pakzad, A. F. Marshall, J. S. Harris, W. Cai and P. C. McIntyre, *Mater. Today*, 2020, 40, 101–113.
- 21 A. Davtyan, T. Krause, D. Kriegner, A. Al-Hassan, D. Bahrami, S. M. Mostafavi Kashani, R. B. Lewis, H. Küpers, A. Tahraoui, L. Geelhaar, M. Hanke, S. J. Leake, O. Loffeld and U. Pietsch, *J. Appl. Crystallogr.*, 2017, **50**, 673–680.
- 22 J. R. Sánchez-Pérez, C. Boztug, F. Chen, F. F. Sudradjat, D. M. Paskiewicz, R. B. Jacobson, M. G. Lagally and R. Paiella, *Proc. Natl. Acad. Sci. U. S. A.*, 2011, 108, 18893.
- 23 E. Kasper, M. Kittler, M. Oehme and T. Arguirov, *Photonics Res.*, 2013, 1, 69–76.